

## Mid-Twenty-First-Century Changes in Extreme Events over Northern and Tropical Africa

EDWARD K. VIZY AND KERRY H. COOK

*Department of Geological Sciences, Jackson School of Geosciences, The University of Texas at Austin, Austin, Texas*

(Manuscript received 28 November 2011, in final form 16 February 2012)

### ABSTRACT

Changes in rainfall and temperature extremes are predicted by many global climate models as a response to greenhouse gas increases, and such changes will have significant environmental and social impacts. A regional climate model is used to predict changes in extremes across tropical and northern Africa for 2041–60 under a midline emissions forcing scenario. Six indicators are examined, including annual extreme and daily diurnal temperature ranges, heat wave days, number of dry days, number of extreme wet days, and extreme wet day rainfall intensity. Confidence in the projections is evaluated by examining the ensemble spread and the validation of extreme events in the twentieth-century simulation.

Despite an increase in both daily minimum and maximum temperatures, diurnal temperature ranges decrease from West Africa to Ethiopia during spring and fall, over the Sahel during summer, and over the Congo basin during winter and spring. Diurnal temperature ranges increase over the Horn of Africa during boreal winter and over Kenya and Tanzania during boreal summer. The number of heat wave days increases north of 8°N with the largest increase (60–120 days) over the western Sahel. The number of dry days decreases over the Congo and the central Sahel but increases over East Africa, the latter associated with a reduction in the springtime long rains. The number of extreme wet rainfall days is projected to increase over West Africa, the Sahel, and the Ethiopian Highlands but decrease over the Congo. The predicted changes in extreme wet rainfall intensity are highly regional.

### 1. Introduction

Future changes in extreme events, including droughts and intense rainfall, will have significant impacts on the environment and society. This is especially true over Africa, as the continent is thought to be particularly susceptible given a high vulnerability to climate variability and relatively low adaptive capacity. Mid-twenty-first-century climate projections on regional space scales are needed to improve our understanding of future changes and allow for better planning to help mitigate impacts over Africa. Coupled atmosphere–ocean global circulation models (AOGCMs) being run in advance of the Intergovernmental Panel on Climate Change (IPCC) Fifth Assessment Report (AR5) are one source of information, but the horizontal space scales of these models, generally about 200 km, may not be ideally suited to evaluate changes in extreme events locally. Regional climate

modeling can increase this resolution to capture extreme events more accurately. In addition, the regional modeling approach allows one to choose parameterizations that work well in the region of interest.

The purpose of this study is to evaluate changes in temperature and precipitation extremes over northern and tropical Africa for the mid-twenty-first century due to increased CO<sub>2</sub> forcing/global warming using a regional climate model, and to evaluate confidence in those predictions. The simulation design differs from traditional dynamic downscaling methods in which boundary conditions are taken from a global climate model. In this study, late-twentieth-century boundary conditions are derived from reanalysis data, while mid-twenty-first-century boundary conditions are generated by adding anomalies generated from AOGCMs to the late twentieth-century boundary conditions generated from the reanalysis. This method increases the accuracy of the twentieth-century simulation and limits the influence of AOGCM errors in the regional model. Rather than providing a direct downscaling of the AOGCM results, these regional model simulations are providing a projection that is more independent of the GCMs and,

---

*Corresponding author address:* Edward K. Vizy, Jackson School of Geosciences, The University of Texas at Austin, 1 University Station C1100, Austin, TX 78712.  
E-mail: ned@jsg.utexas.edu

therefore, more valuable in assessing confidence through multimodel comparisons.

The background is reviewed in section 2. A description of the regional climate model and experimental design are presented in section 3a. The extreme weather indicators used are described in section 3b, and the evaluation of confidence is addressed in section 3c. A validation of each indicator is presented in section 4 along with an evaluation of its mid-twenty-first-century prediction. Conclusions are summarized in section 5.

## 2. Background

The frequency and intensity of extreme events are expected to change as the climate warms under greenhouse gas forcing [see the IPCC Fourth Assessment Report (AR4), Meehl et al. (2007)], including more frequent and persistent heat waves, a decrease in the diurnal temperature range, increased summer dryness, and increased intense precipitation and flooding.

Post-IPCC AR4 research on changes in extremes specific to tropical and northern Africa is limited, often focused on the end of the twenty-first century when the climate change signal is more clearly distinguished from the background variability. Shongwe et al. (2011) evaluate twenty-first-century changes in extreme rainfall over Kenya, Uganda, and Tanzania using Coupled Model Intercomparison Project Phase 3 (CMIP3) atmosphere–ocean global circulation model (AOGCM) output under the A1B emissions scenario. They find an increase in mean rainfall rates and high intensity events for the end of the century, especially during boreal fall short rains. Sylla et al. (2010) analyze projections from a regional model constrained by the ECHAM5 AOGCM for the end of the twenty-first century under the A1B forcing scenario and find an increased likelihood of dry spells over the western Sahel and West Africa.

Patricola and Cook (2010, 2011) evaluate late twenty-first century regional climate model projections run under the A2 “business as usual” emissions scenario. Their model predicts wetter conditions during boreal spring over West Africa, but midsummer drying develops during June and July accompanied by increased risk of heat stroke over the Sahel. During late summer, wetter conditions resume, increasing the risk for flooding and higher intensity rainfall events along the Guinean coast.

Paeth and Thamm (2007) use a regional model to examine changes in extreme events over tropical and sub-Saharan Africa until 2025 under the A1B emissions scenario. Their projections indicate that tropical Africa is likely to be drier in the future with less severe rainfall extremes during boreal summer but with more intense heat waves. In another regional modeling study with

future land-cover changes included, Paeth et al. (2009) project significantly longer dry spells until 2050 over tropical and sub-Saharan Africa. Paeth et al. (2011) examine the changes in annual precipitation during the 2001–50 period from 10 different regional climate models from the Ensembles-based Predictions of Climate Changes and Their Impacts (ENSEMBLES) Africa project. While the average results indicate a drying tendency in sub-Saharan Africa, there is a large spread among models. Vigaud et al. (2011) use a regional model to downscale low-resolution GCM projections over West Africa for 2032–41 under the A2 emissions scenario. They find that rainfall patterns produced by the regional model over sub-Saharan western and central Africa are more realistic than the GCM, with an improved representation of less intense rainfall events. Their regional model predicts a significant increase in boreal summer rainfall over the central Sahel and a general warming of the surface by 1–2 K during 2032–41.

The studies discussed above provide a basis for beginning to understand how extreme events may change in the future over Africa as they provide information related to changes in temperature and/or precipitation extremes in some manner. However, these studies do not always provide analysis for the same period in time nor do they examine the same extreme indicators making it difficult to thoroughly and confidently evaluate how extreme events will change at midcentury. This study attempts to bridge this gap by providing a detailed regional analysis of extreme indicators relevant to sub-Saharan northern and tropical Africa on annual to monthly time scales produced by a higher-resolution regional climate model.

## 3. Methodology

### a. Regional climate model simulations

The regional climate model simulations evaluated in this study are the same as those analyzed in Cook and Vizu (2012). Below is a brief description of the simulation design. For a complete description and comprehensive validation please see Cook and Vizu (2012).

The National Center for Atmospheric Research–National Oceanic and Atmospheric Administration (NCAR–NOAA) Weather Research and Forecasting (WRF) (Skamarock et al. 2005) regional model V3.1.1 is used with a time step of 180 s, horizontal resolution of 90 km, and 32 vertical levels. The top of the atmosphere is set at 20 hPa. This resolution is chosen because previous studies (Patricola and Cook 2010, 2011) demonstrate that the model can realistically simulate the African climate at this resolution.

A large model domain is selected (Fig. 1). The lateral boundaries are positioned far away from Africa to provide

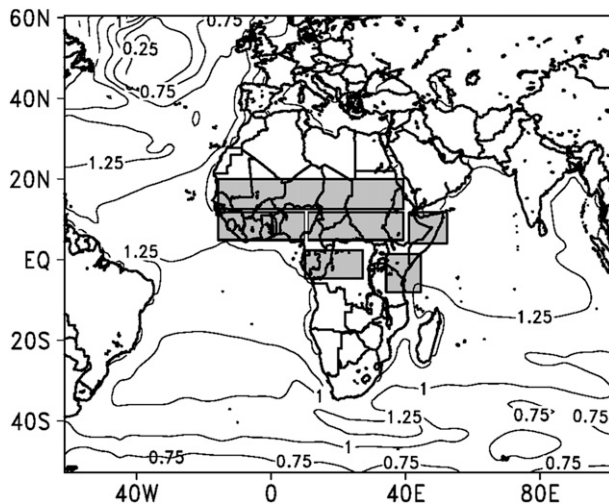


FIG. 1. The 90-km resolution model domain and 21C annual SSTAs (K). Boxes denote averaging regions used in the analysis and include the Sahel (12.5°–20.0°N, 15.7°W–39.4°E), West Africa (4.9°–11.7°N, 15.7°W–10.1°E), Central Africa (4.9°–11.7°N, 11.0°–39.4°E), Horn of Africa (4.0°–11.7°N, 41.1°–52.3°E), Congo (4.6°S–2.3°N, 10.1°–27.3°E), and Tanzania–Kenya (8.0°S–1.4°N, 34.2°–44.6°E).

ample space for the development of subtropical anticyclones over the adjacent oceans and to minimize the effects of their constraints in the analysis region. Physical parameterizations chosen include the Yonsei University planetary boundary layer (Hong et al. 2006), Monin–Obukhov surface layer, new Kain–Fritsch cumulus convection (Kain 2004), Purdue–Lin microphysics (Chen and Sun 2002), the Rapid Radiative Transfer Model (RRTM) longwave radiation (Mlawer et al. 1997), the Dudhia shortwave radiation (Dudhia 1989), and the unified Noah land surface model (Chen and Dudhia 2001).

An ensemble approach is applied to improve the reliability of the simulations and provide a tool for evaluating confidence. Two ensembles, each consisting of six year-long simulations, are constructed. The first represents the late twentieth century (1981–2000) and is referred to as “20C.” Initial, surface, and lateral boundary conditions are derived from the 1981–2000 monthly climatology of the National Centers for Environmental Prediction reanalysis 2 (NCEP2) (Kanamitsu et al. 2002). Lateral boundary conditions are updated every 6 h using the NCEP2 climatology interpolated onto the boundaries. The monthly means are assumed to represent the middle of the month, and linear interpolation is used to generate boundary conditions every 6 h. These boundary conditions include seasonality, but shorter time scales are filtered out. This “climate mode” methodology has been demonstrated to be useful in past regional modeling studies over Africa and the adjacent

oceans (e.g., Vizy and Cook 2002, 2003; Hagos and Cook 2007; Patricola and Cook 2007, 2010, 2011).

The six 20C ensemble members differ in their initial conditions. They are taken from two 3-yr integrations that are initialized at 0000 UTC 1 March and 0000 UTC 15 March, respectively. Each 3-yr integration is spun up until the following 1 January to allow the subsurface soil moisture and soil temperature to equilibrate with the climate. (For computational efficiency, each of the six ensemble members is not spun up individually.) The six members are treated and analyzed as independent annual simulations, and simulations from one 3-yr run do not tend to cluster (Cook and Vizy 2012). Model output is written every 3 h for analysis.

The second ensemble represents the mid-twenty-first century (2041–60) under the IPCC AR4 A1B emissions scenario and is referred to as “21C.” CO<sub>2</sub> concentrations are adjusted from late twentieth-century values to 536 ppmv, which represents the 2041–60 average under the A1B emissions scenario. Effects of other greenhouse gases and aerosols are not included. SSTs, initial, and lateral boundary conditions for the 21C simulations are derived from a coupled atmosphere–ocean GCM (AOGCM) and applied as anomalies to the 20C boundary conditions from the reanalysis. The AOGCM anomalies are calculated as the differences between the monthly mean, A1B-forced simulations averaged over 2041–60 and monthly mean historical simulations averaged over 1981–2000. These anomalies are interpolated to the NCEP2 reanalysis grid, added to the reanalysis climatological monthly values, and linearly interpolated to form 6-hourly values. The 20C soil moisture initialization values are used for the 21C simulations, and the six members of the ensemble are generated in the same way as for the 20C ensemble.

Output from nine AOGCMs prepared for the CMIP3 multimodel dataset (Meehl et al. 2007) are used to generate the future anomalies by formulating a multimodel ensemble mean difference. Multimodel mean anomalies are used to reduce the dependence of the projections on individual AOGCMs. The models used include the Canadian Centre for Climate Modeling and Analysis Coupled General Circulation Model, version 3.1 [CGCM3.1 (T47)]; the Centre National de Recherches Météorologiques Coupled Global Climate Model, version 3 (CNRM-CM3); the Max Planck Institute for Meteorology Ocean Model (ECHAM5/MPI-OM); the NOAA/Geophysical Fluid Dynamics Laboratory (GFDL) Climate Model, version 2.0 (CM2.0); the Model for Interdisciplinary Research on Climate 3.2, medium-resolution version [MIROC3.2(medres)]; the Meteorological Research Institute Coupled General Circulation Model, version 2.3.2 (MRI-CGCM2.3.2); the NCAR Community

Climate System Model, version 3 (CCSM3); the NCAR Parallel Climate Model (PCM); and the third climate configuration of the Met Office Unified Model (HadCM3).

### b. Indicators of extreme weather

Six main indicators of climate extremes are evaluated.

The *extreme temperature range* is the difference between the warmest daily maximum temperature of the year minus the coldest daily minimum temperature of the year. It provides a simple measure of temperature range (Frich et al. 2002; Tebaldi et al. 2006).

The *daily diurnal temperature range* is defined in the statistical software package RCLimDex, developed at the Climate Research Branch of the Meteorological Service of Canada (Zhang and Yang 2004). This indicator is the difference between the maximum temperature and the minimum temperature for a given day. Unlike its use in RCLimDex, this measure is not averaged into monthly means here. This indicator provides daily to seasonal information about how temperature ranges change, which supports the interpretation of simulated changes in the extreme temperature range.

Predicting *heat wave days* is important because hot spells are often associated with mortality statistics, but there is no universally applied definition of a heat wave (Robinson 2001). Frich et al. (2002) define a heat wave as at least five consecutive days with the maximum temperature 5°C greater than the climatological daily normal. In RCLimDex (Zhang and Yang 2004), a warm spell is at least six consecutive days when the maximum temperature exceeds the 90% percentile of the daily normal. The issue with these “deviation from the normal” heat wave measures is that they may or may not be associated with health-related/mortality issues because universal biological factors contribute to the specification of healthy temperatures.

Other definitions, such as the one employed by the U.S. National Weather Service (NWS), define heat waves based on the exceedence of a fixed value that represents a lower physiological limit threshold (Robinson 2001). The NWS uses the maximum apparent temperature, which factors in temperature and relative humidity to identify extreme days that are of concern for human health.

The indicator evaluated in this study is based on apparent temperature, similar to the NWS method. Here, apparent temperature,  $T_a$ , is defined as in Steadman (1979, 1984) by

$$T_a = -2.07 + 1.04T + 2.0e - 0.65v_{10}, \quad (1)$$

where  $T$  is air temperature,  $e$  is vapor pressure (kPa), and  $v_{10}$  is the 10-m wind speed. The maximum daily

apparent temperature is determined and a heat wave is defined when the daily maximum apparent temperature is greater than or equal to 314.15 K (41°C) for at least three consecutive days. The threshold of 41°C represents the point when heat cramps and heat exhaustion are likely, with heat stroke probable with continued activity based on the NWS scale. A duration of at least three consecutive days is chosen based on evidence that mortality is more likely by the third day under such conditions (Kalkstein and Smoyer 1993).

The *number of dry days* is the number of days per year when the daily rainfall rate is less than 1 mm. Unlike comparable measures, for example, those used by Frich et al. (2002), Zhang and Yang (2004), and Tebaldi et al. (2006), the days need not be consecutive as the simulation design described in section 2a is not appropriate for evaluating dry periods that extend multiple years.

The *number of extreme wet days* counts the number of days per year when the daily rainfall rate exceeds a threshold. Two threshold values are used. One is the 95th percentile (Frich et al. 2002; Zhang and Yang 2004) and the other is  $1.5 \times$  interquartile range (IQR) of the local rainfall distribution (Moore and McCabe 1993).

The *extreme wet day rainfall intensity* is the average daily rainfall rate of the extreme wet days based on the two thresholds discussed above. It is calculated by dividing the annual accumulated daily rainfall associated with extreme wet days by the number of extreme wet days.

### c. Evaluating confidence

Confidence in the simulations is evaluated by the following methods:

- The quality of the 20C simulation is evaluated to assess how realistically the model can reproduce the six indicators of extreme events discussed above. A reasonable representation of these indicators is viewed as a necessary but not sufficient condition for a confident prediction. Multiple datasets are used for validation so uncertainty in the observations and reanalyses can be factored into the validation process. For the extreme indicators dependent on temperature the NCEP2 and the ECMWF Re-Analysis Interim (ERA-I) reanalyses are used, while precipitation-based indicators are validated against the NASA Global Precipitation Climatology Project (GPCP) 1° daily rainfall dataset and the NASA Tropical Rainfall Measuring Mission (TRMM) 0.25° resolution 3B42V6 rainfall estimate.
- The degree of agreement among individual ensemble members for extreme event indicators is assessed. More confidence is placed in a projection when there

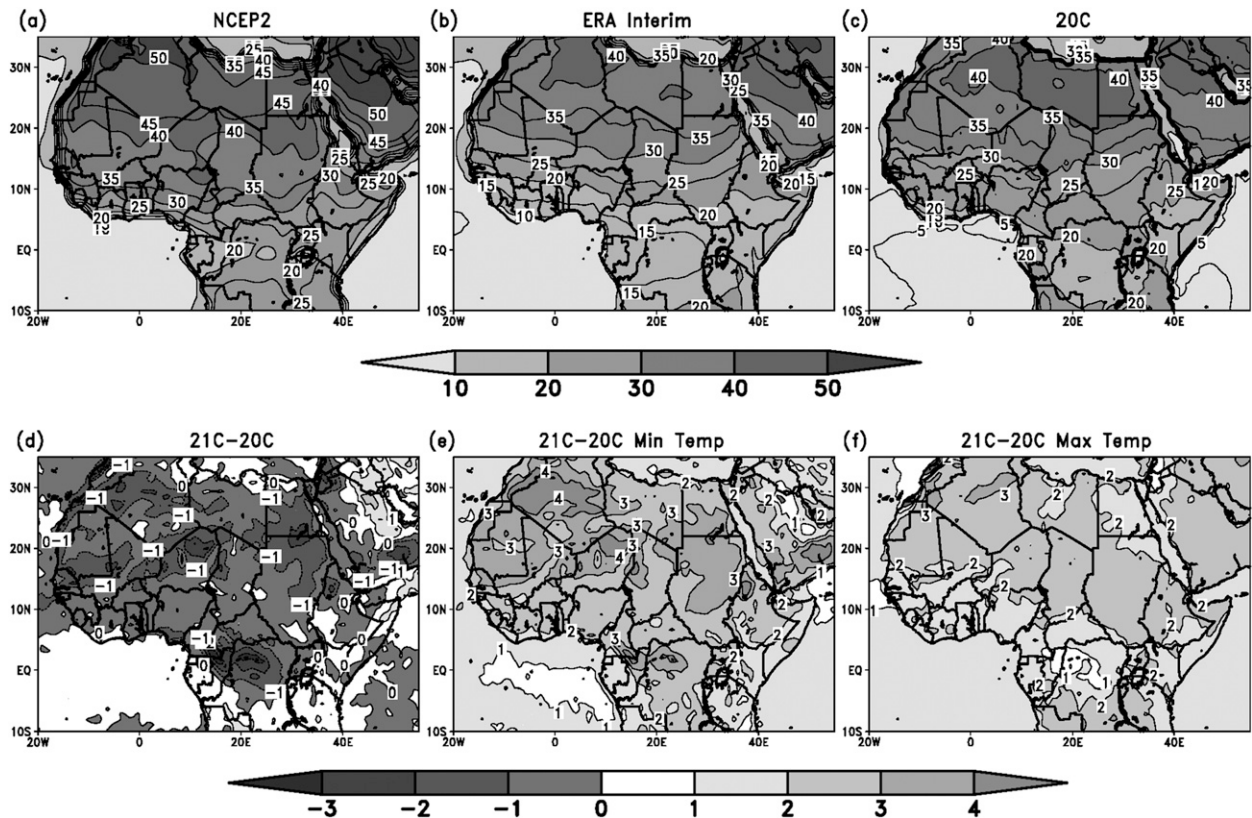


FIG. 2. Average annual extreme temperature range from the (a) NCEP2 reanalysis (1989–2009 average), (b) ERA-Interim reanalysis (1989–2009 average), and (c) 20C (six-member ensemble mean). The 21C minus 20C average annual (d) extreme temperature range, (e) minimum temperature, and (f) maximum temperature differences. Units are K.

is good agreement among the members and vice versa.

- Results are compared with other modeling studies for the mid-twenty-first century when available.

## 4. Results

### a. Extreme temperature range

Figures 2a and 2b show the average annual extreme temperature range from the NCEP2 and ERA-I reanalyses. A band with small temperature ranges crosses the continent between 8°S and 5°N. Both reanalyses place the lowest ranges, below 20 K in NCEP2 and below 15 K in ERA-I, over the Congo basin centered on the equator and extending into a narrow region along the Guinean and Somali coasts. The range increases northward from the equator and is fairly zonally uniform. It reaches a maximum greater than 45 K over Algeria. The two reanalyses differ in the magnitude of this maximum with NCEP2 values approximately 10 K larger than those in the ERA-I reanalysis. Note NCEP2 is known to have a cold and wet bias over the Sahara

and Sahel (Betts et al. 2006; Kharin et al. 2007). Over southern Ethiopia, Somalia, and Kenya the temperature range varies between 15 and 25 K.

Figure 2c shows the average annual extreme temperature range from the 20C ensemble mean. Overall, the simulated range is consistent with the reanalysis ranges, but it is in better agreement with the ERA-I values than the NCEP2 values. This includes a more modest range of 25–30 K over the southern Sahel (10°–15°N) compared to the 35–40-K range in the NCEP2 reanalysis.

Figure 2d shows the difference in extreme temperature range for the 21C–20C ensemble means, and Figs. 2e and 2f show 21C–20C differences in the average minimum and maximum annual temperatures, respectively. There is a projected decrease in the future extreme temperature range over all of tropical and northern Africa, and there is no discernible latitudinal dependence of the difference field (Fig. 2d). The largest reductions, over 4 K, occur over the Congo. Over the Sahel (10°–20°N) there is a 2–3-K decrease, while over the Sahara there are regional decreases including over Algeria (1–3 K) and Egypt (1–2 K). Both annual minimum and maximum temperatures increase in the future (Figs. 2e and

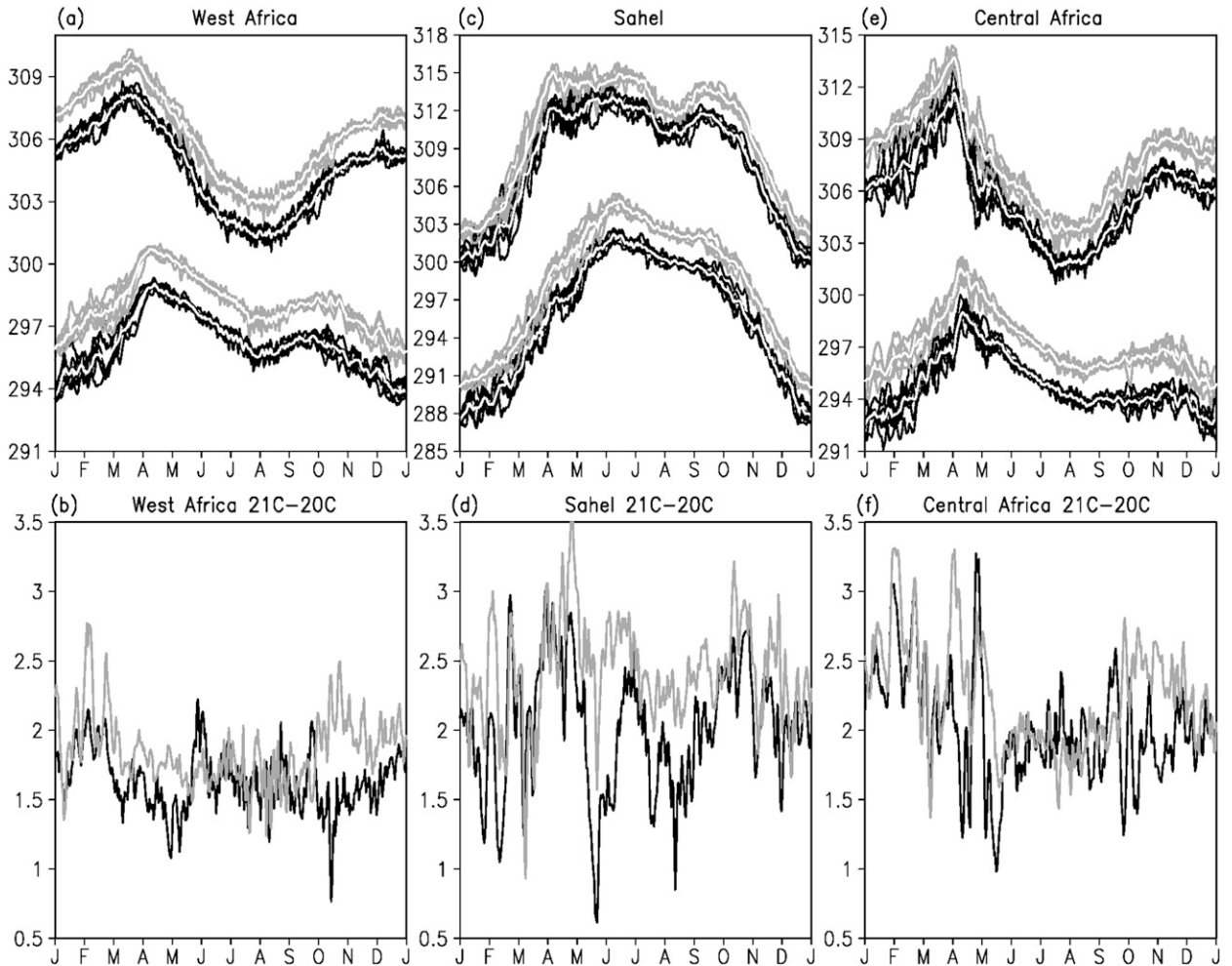


FIG. 3. Regional daily maximum and minimum temperatures for the 20C (black) and 21C (gray) simulations for the (a) West Africa, (c) Sahel, and (e) Central Africa regions. Shading denotes individual ensemble members while white lines denote ensemble means. The 21C–20C ensemble mean regional daily maximum (black) and minimum temperatures (gray) differences for the (b) West Africa, (d) Sahel, and (f) central Africa regions. Units are K.

2f) but the increase in the minimum temperature is generally greater than the increase in the maximum temperature, consistent with greater warming at night and observed trends (e.g., Vose et al. 2005).

Figure 3 shows 20C and 21C daily minimum and maximum temperatures for the West Africa, Sahel, and Central Africa averaging regions (Fig. 1). Values from each ensemble member are plotted using black (20C) and gray (21C) lines, and the ensemble mean is indicated by the white lines embedded among the values from the ensemble members. Over West Africa (Figs. 3a,b) the increase in minimum temperature is greater than the increase in maximum temperature from February to mid-May and from mid-October through December, resulting in 0.5–1.5-K decreases in the daily temperature range. During the West African monsoon season (mid-May–mid-September) there is little predicted change in

the daily temperature range. Note there is good agreement among individual ensemble members (Fig. 3a). The spread in daily maximum and minimum temperatures is generally less than  $\pm 1$  K, and all 20C ensemble members are clearly distinguished from all of the 21C ensemble members. The 1.5–2.5-K increase in the maximum and minimum temperature (Fig. 3b) is consistent with the mid-twenty-first-century increase projected by the IPCC AR4 (Meehl et al. 2007) and regional modeling studies (Paeth and Thamm 2007; Vigaud et al. 2011).

Over the Sahel (Figs. 3c,d) minimum temperatures warm more than maximum temperatures for most of the year, suggesting that the global warming temperature signal is greater during the night. The largest decreases in the daily temperature range (i.e., 0.5–1.8 K) are projected for May/early June, and August/September. Both the

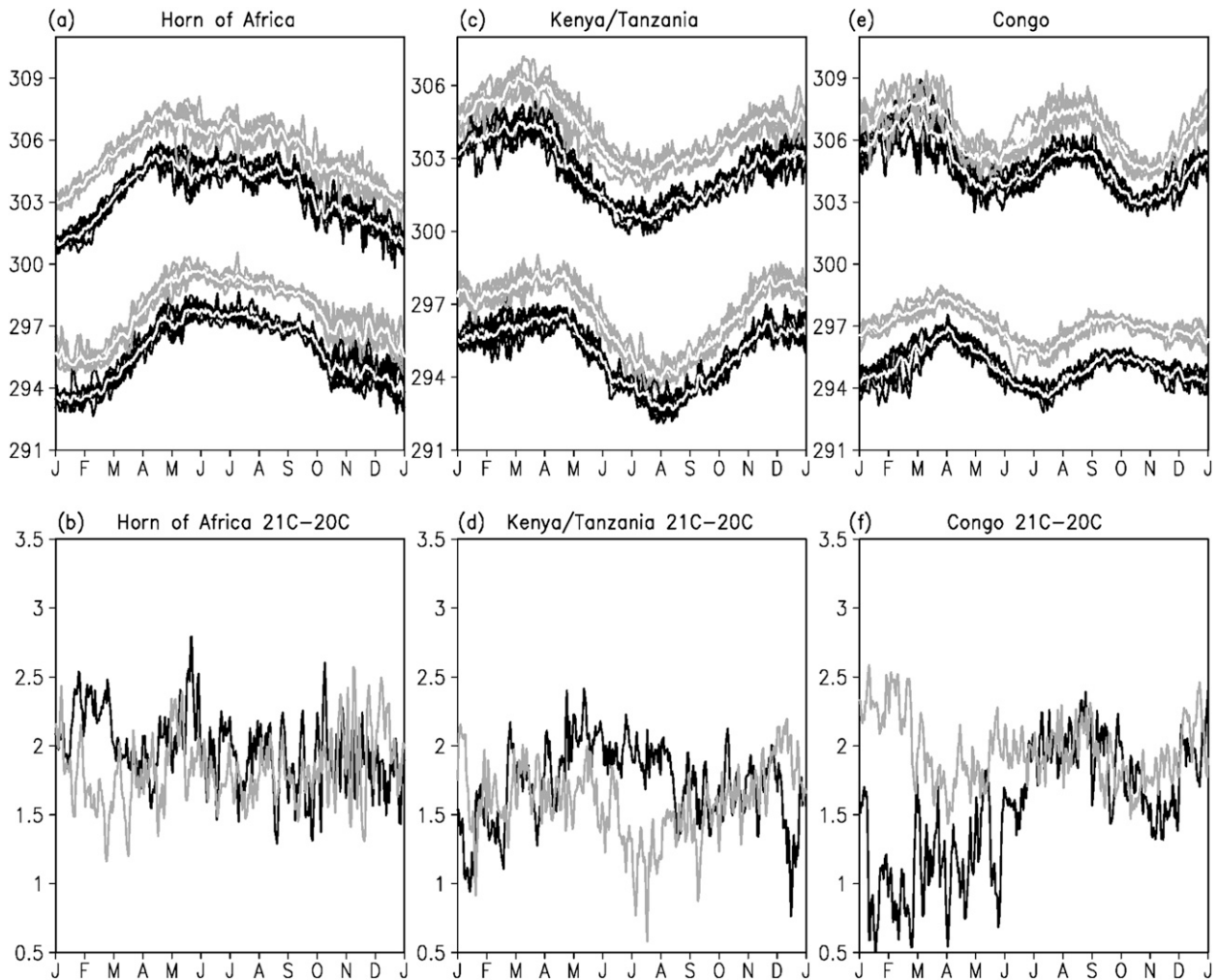


FIG. 4. Regional daily maximum and minimum temperatures for the 20C (black) and 21C (gray) simulations for the (a) Horn of Africa, (c) Kenya-Tanzania, and (e) Congo regions. Shading denotes individual ensemble members while white lines denote ensemble means. The 21C-20C ensemble mean regional daily maximum (black) and minimum (gray) differences for the (b) Horn of Africa, (d) Kenya-Tanzania, and (f) Congo regions. Units are K.

May/June and August/September changes are associated with an increase in rainfall over the Sahel and a strengthening of the thermal low over the Sahara [see Figs. 7c and 8b in Cook and Vizy (2012)]. The projected 1.5–3-K increase in the minimum and maximum temperatures agrees with the mid-twenty-first-century IPCC AR4 AOGCM A1B projections of 2–2.5-K warming (Meehl et al. 2007).

Farther south, over the Central Africa region (Figs. 3e,f), the largest decreases in the daily temperature range (0.4–1.5 K) occur during April and October/November. Daily maximum and minimum temperatures warm by 1.5–2 K during boreal summer, up to 2.5 K in boreal fall, and up to 3 K in boreal winter. For comparison, the IPCC AR4 AOGCMs project an annual warming of 1.5–2 K over this region (Meehl et al. 2007).

Figures 4a and 4b show the 20C and 21C daily minimum and maximum temperatures and their differences over the Horn of Africa averaging region. Here there is a predicted increase in the daily temperature range during mid-January through March, associated with an approximate 20% decrease in low-level relative humidity (not shown). Minimum and maximum temperatures are predicted to warm by 1.5–2.5 K, consistent with IPCC AR4 mid-twenty-first-century A1B annual projections for the region (Meehl et al. 2007).

Over the Kenya-Tanzania region (Figs. 4c,d), there is a predicted increase in the daily temperature range from mid April until mid August as the low to midlevel relative humidity is projected to decrease by 10%–20%. This is associated with a weakening of the easterly flow and moisture transport from the Indian Ocean (not shown).

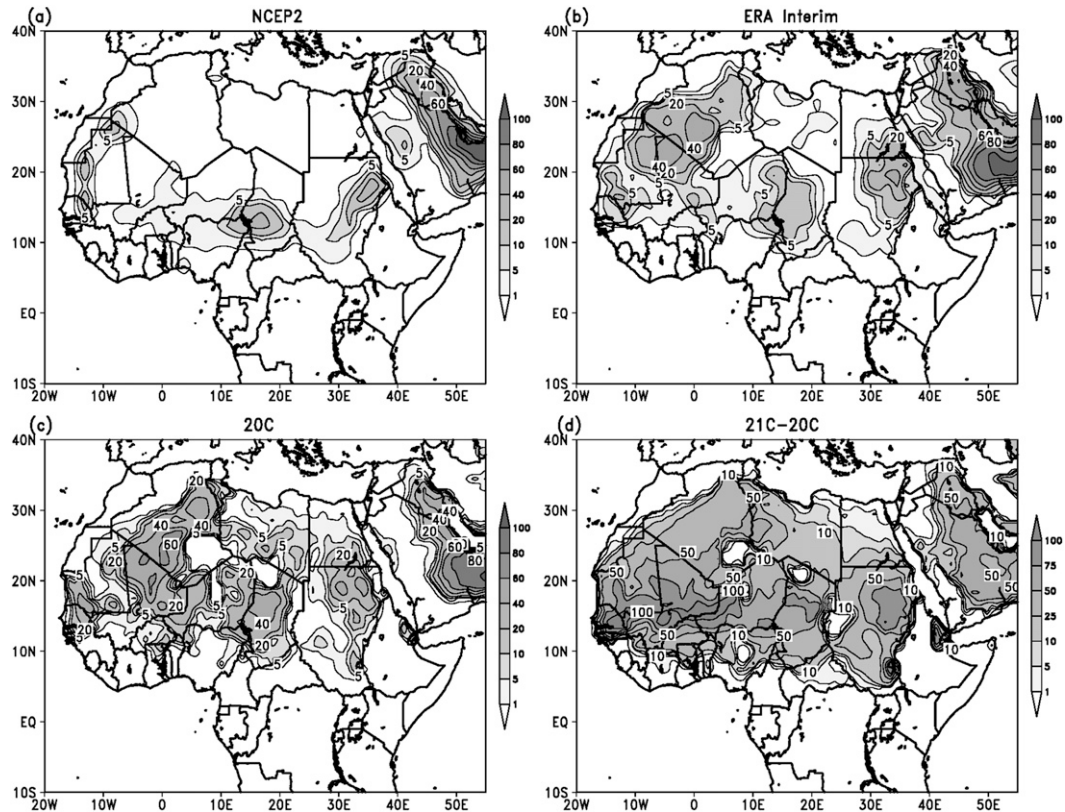


FIG. 5. Average number of heat wave days per year from the (a) NCEP2 reanalysis (1989–2009 average), (b) ERA-Interim reanalysis (1989–2009 average), and (c) 20C ensemble (six-member average). (d) 21C minus 20C difference in the average number of heat wave days per year.

The future increase in daily minimum temperature over the Congo region (Figs. 4e,f) is predicted to be larger than the increase in the maximum temperature during the boreal winter and spring months, indicating a reduced daily temperature range. The largest differences of up to 2 K occur during January–February. This change coincides with at least a doubling of the 21C precipitation over the Congo region during this time (see Fig. 11c in Cook and Vizy 2012). Paeth and Thamm (2007) also predict weaker warming over a large part of the Congo basin during the boreal winter months compared to the rest of the year in their 2000–25 regional climate model simulations.

### b. Heat wave days

Figures 5a and 5b show the number of heat wave days per year calculated from the NCEP2 and ERA-I reanalyses for 1989–2009. Both reanalyses have a maximum across the Sahel, with up to 20 heat wave days per year. Local maxima are located over northeastern Sudan, the Bodélé region of Chad, southwestern Niger/northern Burkina Faso, and northern Senegal/southern Mauritania. Over the northwestern Sahara, including Algeria,

Mauritania, and northern Mali, the two reanalyses disagree, with relatively few heat wave days in the NCEP2 reanalysis compared to 40–60 days  $\text{yr}^{-1}$  in the ERA-I reanalysis.

Figure 5c shows the 20C ensemble-mean number of heat wave days per year. The regional model reproduces the location of the heat wave day maxima across the Sahel. Similar to the ERA-I reanalysis, the regional model produces a maximum over the northwestern Sahara of Algeria, northern Mali, and eastern Mauritania, but the number of days predicted is approximately 5–10 more than observed from the ERA-I reanalysis. Likewise, the regional model tends to simulate more heat wave days compared to the ERA-I over Libya and Egypt.

Figure 5d shows the ensemble mean difference, 21C – 20C, in the number of heat wave days simulated. The average number of heat wave days increases across the Sahel, with the largest rise (80–120 days) occurring over the western Sahel between 12° and 18°N from Senegal to Niger. The projected increase in the number of heat wave days over the Sahel occurs in every month from March through October (not shown). There is also a predicted increase in the number of heat wave days over

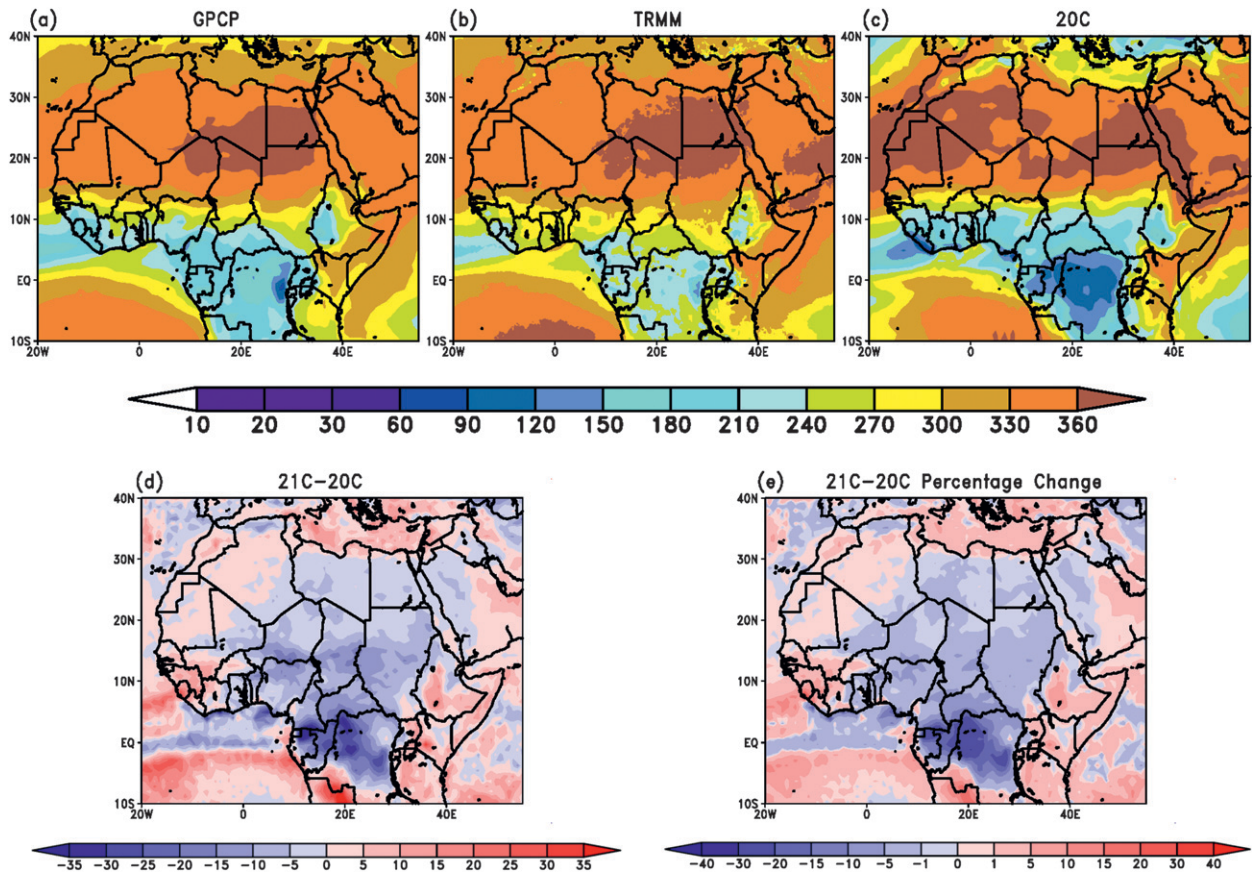


FIG. 6. Average number of days per year when the daily rainfall is less than  $1 \text{ mm day}^{-1}$  in the (a) 1997–2008 GPCP  $1^\circ$  daily precipitation climatology, (b) 1998–2010 TRMM climatology, and (c) 20C ensemble (six-member average). The (d) difference for 21C minus 20C in the number of days per year when the daily rainfall is less than  $1 \text{ mm day}^{-1}$  and the (e) 21C minus 20C percent change difference.

northern West Africa and the Central Africa averaging regions (between  $8^\circ$ – $11^\circ\text{N}$ ). This increase occurs during boreal spring with a peak in April, a time when the solar insolation is moving north of the equator and the low-level atmospheric moisture content is building, but the high rainfall rates of the monsoon have not yet begun.

These mid-twenty-first-century heat wave projections agree with the Patricola and Cook (2010) late twenty-first-century A2 scenario heat index projections in that the largest increase in heat wave days that impact human health occurs across the entire Sahel and, to a lesser extent, over the western Sahara in southern Algeria and northern Mali. The increase in the number of heat wave days over the Horn of Africa region, with both TRMM and GPCP data indicating greater than 330 dry days. However, the spatial coverage of the number of dry days greater than 330 days is more widespread over Somalia and eastern Ethiopia in TRMM.

These mid-twenty-first-century heat wave projections agree with the Patricola and Cook (2010) late twenty-first-century A2 scenario heat index projections in that the largest increase in heat wave days that impact human health occurs across the entire Sahel and, to a lesser extent, over the western Sahara in southern Algeria and northern Mali. The increase in the number of heat wave days over the Horn of Africa region, with both TRMM and GPCP data indicating greater than 330 dry days. Unlike in Patricola and Cook, there is no evidence of an increase in heat wave days over the Congo basin indicating that the mid-twenty-first-century warming is likely not strong enough as of yet to exceed the threshold.

### c. Number of dry days

Figures 6a and 6b show the number of dry days per year as estimated from the GPCP  $1^\circ$  daily rainfall dataset and the NASA TRMM  $0.25^\circ$  resolution 3B42V6 estimate. Both products agree that the fewest dry days occur over the Congo basin and the West African coast between  $5^\circ$ – $10^\circ\text{N}$  but they disagree on the number of dry days, with the GPCP climatology indicating approximately 50–80 fewer dry days than the TRMM observations. There is a similar disagreement in the number of dry days between the two rainfall products farther north between  $4^\circ$ – $12^\circ\text{N}$ . There is generally good agreement between the two rainfall products farther north between  $4^\circ$ – $12^\circ\text{N}$ . There is generally good agreement between the two rainfall products farther north between  $4^\circ$ – $12^\circ\text{N}$ . There is generally good agreement between the two rainfall products farther north between  $4^\circ$ – $12^\circ\text{N}$ .

The number of dry days simulated in the 20C ensemble mean is shown in Fig. 6c. The overall pattern is realistic, but the regional model does not simulate as

many dry days as in the observations so the agreement with the GPCP data is better than with TRMM. Along the Guinean coast there are 60 to 90 fewer dry days compared with the GPCP. The model captures the Congo basin minimum, but somewhat too strongly. However, the regional model results represent an improvement over the IPCC AR4 AOGCMs, which tend to oversimulate the number of days when the daily rainfall is greater than 1 mm over tropical Africa (not shown).

Figure 6d shows the 21C–20C ensemble mean difference in the number of dry days per year, and Fig. 6e shows the percentage difference. The 21C simulation projects a 5–20-day decrease in the number of dry days between 8°–15°N over Niger, northern Nigeria, Chad, Sudan, and the Central African Republic, which translates into a 3%–7% reduction in the number of dry days. The number of dry days decreases by 15–35 days over the Congo basin, a 15%–25% reduction. Over Guinea, Sierra Leone, southwestern Mali, the Ethiopian Highlands, and central Somalia the number of dry days increases by 5–20 days, a 2%–10% increase.

Figure 7 shows the annual time series of the ensemble-mean number of dry days per month from 20C (black lines) and 21C (gray lines) over the six averaging regions (Fig. 1). In West Africa there is a 5% (15%) decrease in the number of dry days during February (October), which translates to approximately 1.12 (2.94) less dry days in 21C. During May and August there are 2.12 day (+30%) and 1.51 day (+16%) increases in the number of dry days over West Africa. In February and October all six 21C ensemble members fall below the 20C ensemble mean, and in May and August they are all above the 20C mean. The spread among the 21C ensemble members is less than in 20C. Using a Student's *t* test to evaluate statistical significance reveals that the April, May, August, and October differences are significant at the 90% confidence interval.

Over the Sahel (Fig. 7b) there is a 1–2-day decrease in the number of dry days per month between May and August, which is a 3%–8% decrease. The spread between the ensemble members is large for May and June but smaller in July and August when all 21C ensemble members are below (drier than) the 20C ensemble mean. Results are statistically significant at the 80% interval for May and at the 90% level for July and August.

Over Central Africa (Fig. 7c) the differences between 20C and 21C are small except during May and October when there is a 2.56- (33%) and a 1.42-day (6.5%) decrease in the number of dry days. The May 21C ensemble member spread is less than the 20C ensemble mean with results statistically significant at the 90% interval, but in October the 20C and 21C spreads overlap with a statistical significance only at the 80% interval.

Over the Horn of Africa (Fig. 7d) and Kenya–Tanzania (Fig. 7e) regions there is a projected increase in the number of dry days during the April/May long rains and the October short rains, while in December there is a 1–2-day reduction. These changes over the Horn of Africa are not highly statistically significant, but the changes over Kenya–Tanzania in May, June, and December are significant. Over the Congo (Fig. 7f) there is a statistically significant 30%–40% decrease in the number of dry days from January through May. All six 21C ensemble members are below the 20C ensemble mean for this period. This result is consistent with the IPCC AR4 AOGCM model projections (Tebaldi et al. 2006; Meehl et al. 2007), which project a decrease in the number of dry days over the Congo basin by the end of the twenty-first century under the A1B emission scenario.

#### *d. Number of extreme wet days and extreme wet-day rainfall intensity*

As discussed above, two methods are used to define extreme rainfall days. One is rainfall rates that exceed the 95th percentile of daily rainfall intensity. The distribution of the daily rainfall intensity that corresponds to the 95th percentile for the GPCP and TRMM rainfall data are shown in Figs. 8a and 8b. In most regions the threshold rainfall intensity is significantly higher (by 15–30 mm day<sup>-1</sup>) in TRMM compared with GPCP; these differences may be due, in part, to differences in resolution since rainfall rates tend to increase when observed or modeled at higher resolution. In addition to differences in magnitude, there are also some notable differences in the structure of the distribution, for example, over the Gulf of Guinea. However, both GPCP and TRMM place relatively high threshold values along the Guinean coast and over the southern Sahel centered along 14°N with larger magnitudes west of 10°E. This maximum corresponds with the location of the summer storm track of easterly waves and squall line activity. Both datasets also have maxima over the western Congo basin and Kenya, Tanzania, and southern Somalia.

Rainfall intensities that correspond to the 95th percentile in 20C are shown in Fig. 8c. The regional model produces a southern Sahel maximum but it is located approximately 2° of latitude farther south than in the observations. The regional model also captures a local maximum in the Congo basin but underestimates the intensity over the equatorial Atlantic and East Africa. The underestimation over the equatorial Atlantic may be related to the model's dry bias in this region during boreal winter and spring when simulated rainfall rates are 40%–60% lower than in TRMM (see Fig. 4 in Cook and Vizu 2012).

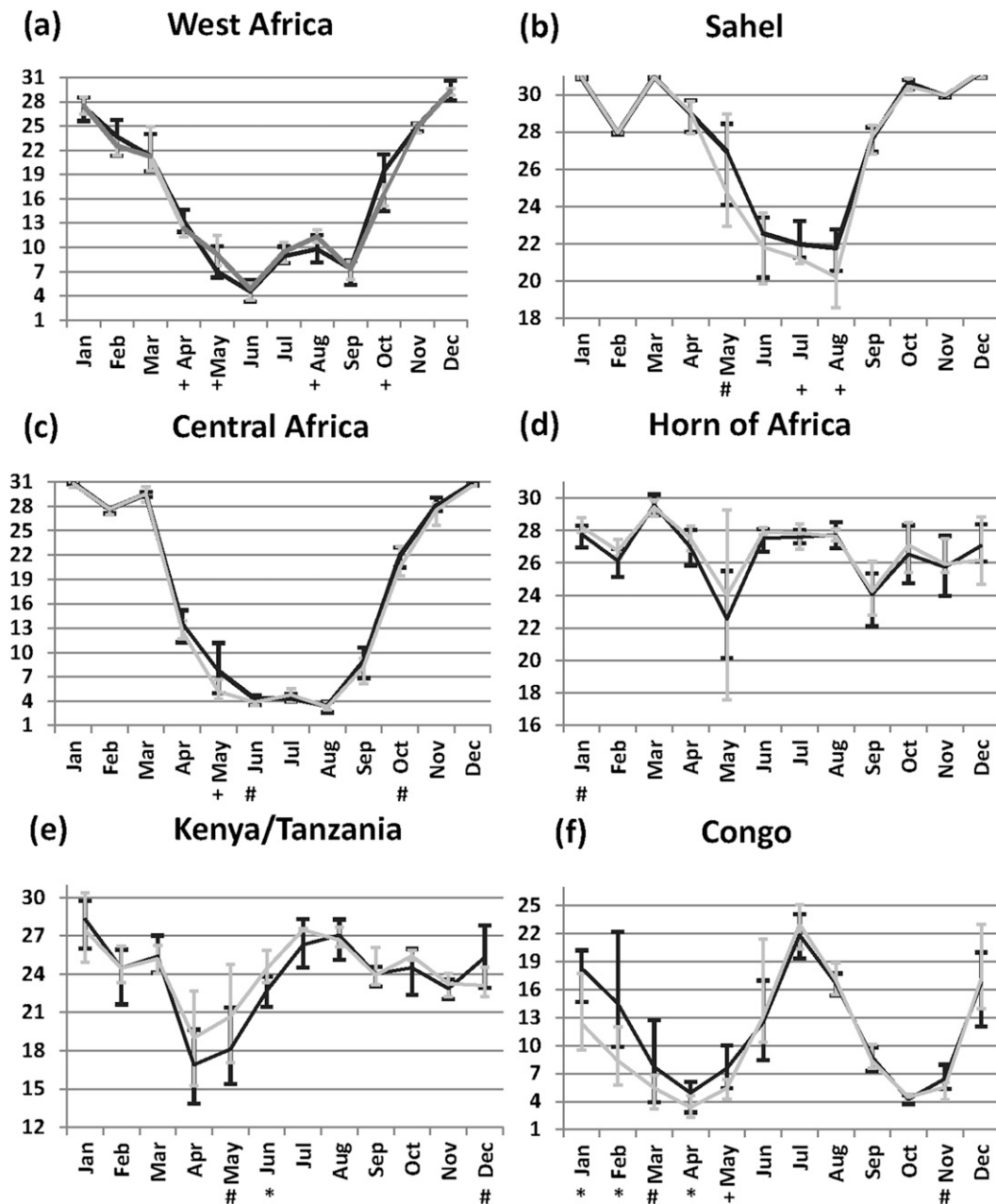


FIG. 7. 20C (black line) and 21C (gray line) ensemble mean average number of dry days per month for the (a) West Africa, (b) Sahel, (c) Central Africa, (d) Horn of Africa, (e) Kenya–Tanzania, and (f) Congo regions. Vertical bars denote the spread of the individual ensemble members. Monthly statistical significance is denoted by the symbols under the  $x$  axis. The #, +, and \* denote statistical significance at the 80%, 90%, and 95% confidence intervals, respectively.

Figures 8d,e show the average number of extreme heavy rainfall days per year using the 95th percentile threshold for the GPCP and TRMM observations. Despite the differences in the magnitude of the 95th percentile intensity (Figs. 8a,b), observed numbers of extreme heavy rainfall days are similar. Both TRMM and GPCP indicate that the highest number of extreme

rainfall days occurs over the eastern Congo basin with numbers ranging from 6–12 days in TRMM to 8–14 days in GPCP. Along the Guinean coast there are generally 4–8 extreme rainfall days, with slightly more days in GPCP than TRMM. The number of extreme rainfall days decreases over the southern Sahel, with none north of about 17°N.

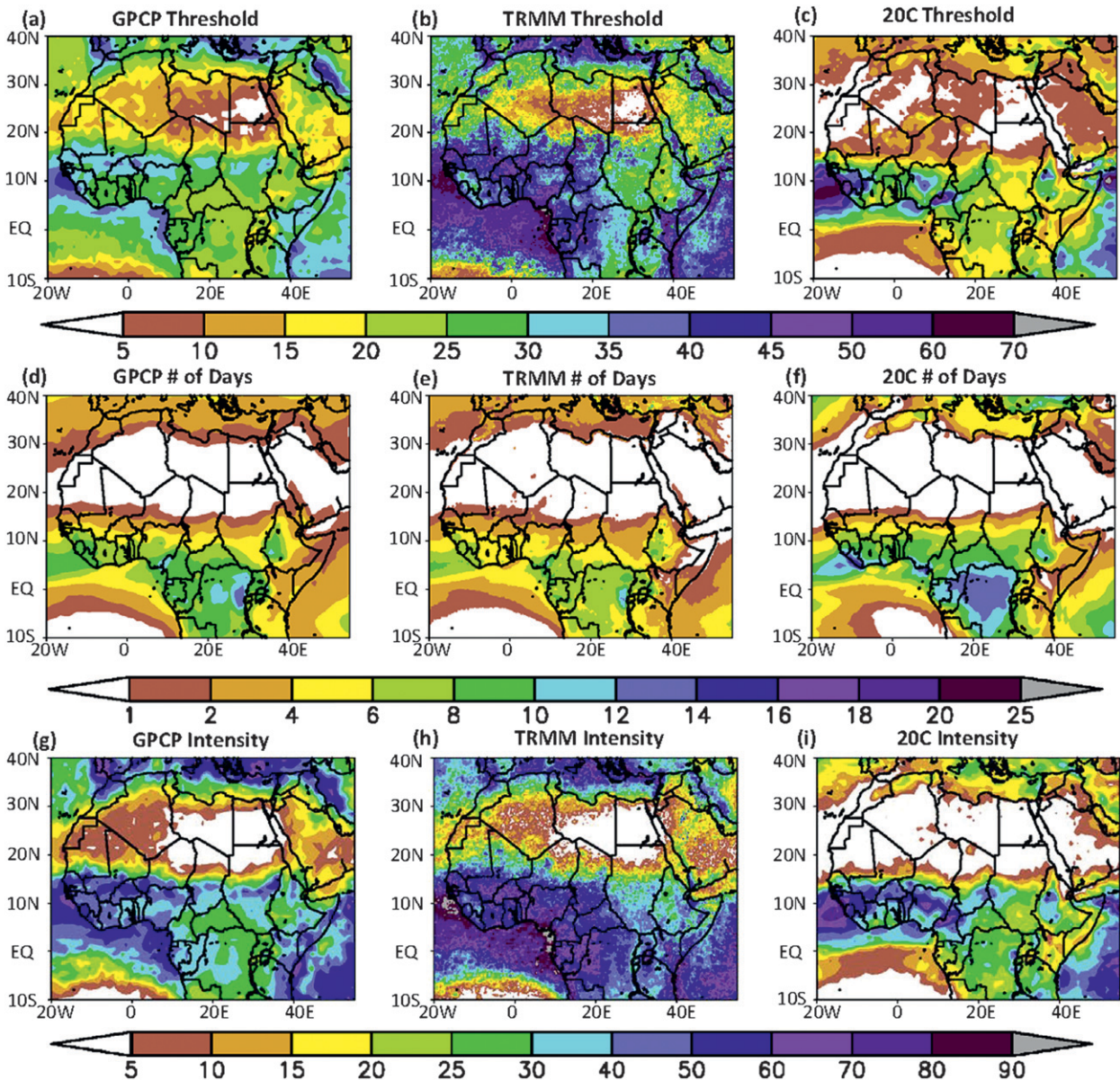


FIG. 8. Extreme daily heavy rainfall threshold ( $\text{mm day}^{-1}$ ) calculated from the (a) 1997–2008 GPCP  $1^\circ$  daily product, (b) 1998–2010 TRMM 3B42V6 product, and (c) 20C ensemble. Threshold is defined as the 95th percentile for rainy days (i.e., daily precipitation  $\geq 1 \text{ mm day}^{-1}$ ). The average number of extreme heavy rainfall days per year for the (d) GPCP, (e) TRMM, and (f) 20C ensemble, and the average rainfall intensity per extreme wet day ( $\text{mm day}^{-1}$ ) for the (g) GPCP, (h) TRMM, and (i) 20C ensemble.

The regional model produces a distribution of the numbers of extreme rainfall days over sub-Saharan northern Africa that is similar to the observations (Fig. 8f), but the model simulates approximately 2 (4) more extreme rainfall days per year over West Africa compared to GPCP (TRMM). Over the Congo basin the regional model simulates approximately 10–14 extreme rainfall days per year compared to 8–12 days in GPCP and 6–8 days in TRMM. The model realistically simulates the number of extreme rainfall days over the East African

coastal plains and the Ethiopian Highlands. The relatively good agreement in the number of extreme wet rainfall days per year between the observations and model indicates that they produce a similar number of events.

Figures 8g–i show the average rainfall intensity of extreme wet rainfall days for the GPCP, TRMM, and 20C simulations, respectively. While the magnitudes differ considerably between the GPCP and TRMM, spatial patterns are similar over some regions. This includes relative maxima over the western Sahel, the Gulf of Guinea

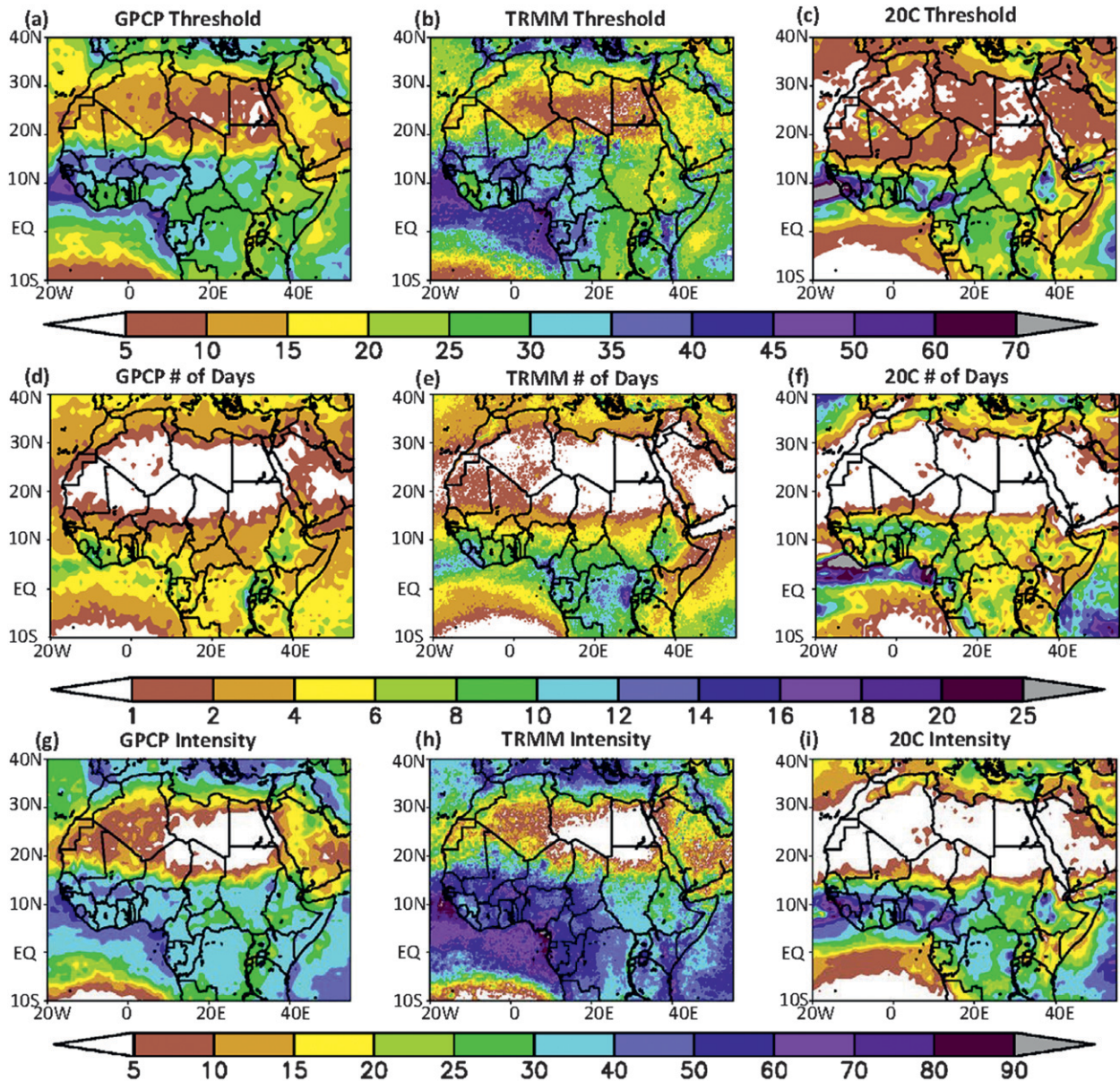


FIG. 9. Extreme daily heavy rainfall threshold ( $\text{mm day}^{-1}$ ) calculated from the (a) 1997–2008 GPCP  $1^\circ$  daily product, (b) 1998–2010 TRMM 3B42V6 product, and (c) 20C ensemble. The threshold is defined as value  $1.5 \times$  interquartile range above the third quartile for wet days (i.e., daily precipitation  $\geq 1 \text{ mm day}^{-1}$ ). The average number of extreme heavy rainfall days per year for the (d) GPCP, (e) TRMM, and (f) 20C ensemble, and the average rainfall intensity per extreme wet day ( $\text{mm day}^{-1}$ ) for the (g) GPCP, (h) TRMM, and (i) 20C ensemble.

north of the equator, and along the Kenyan–Tanzanian coast. The poorest agreement over the land occurs over central Africa and the Congo basin, with GPCP intensities at least half of the TRMM magnitudes. The simulated rainfall intensity from the model (Fig. 8i) generally falls within the observational range, with the distribution more closely resembling GPCP rather than TRMM. The exception is over Somalia, Kenya, and Tanzania where the simulated extreme wet day intensity is much lower than

the observed range reflecting the dry model bias over this region (see Fig. 4 in Cook and Vizi 2012).

In Fig. 9, extreme events are defined using the IQR approach discussed in section 3. Figures 9a,b show the calculated threshold for the GPCP and TRMM data, respectively. The distribution of the threshold intensity is similar to that of the threshold value defined by the 95th percentile in Figs. 8a,b, but with higher values in the southern Sahel, Congo basin, and East Africa. As is the

case when the 95th percentile is used, the higher-resolution TRMM data has overall higher threshold values than the GPCP, but the differences are reduced somewhat when the IQR is used to define extreme events. For example, the IQR threshold value is larger over the Sahel, West Africa, Central Africa, and Congo in the GPCP (cf. Figs. 8a and 9a) and smaller in the TRMM (Figs. 8b and 9b) compared with the 95th percentile values. Over Kenya and Somalia the threshold is approximately  $5 \text{ mm day}^{-1}$  lower in GPCP compared to Fig. 8a, and  $10\text{--}20 \text{ mm day}^{-1}$  lower in TRMM compared to Fig. 8b.

The 20C simulation extreme events defined by the IQR method are shown in Fig. 9c. Again, the location of the southern Sahel maximum is farther south than the TRMM and GPCP maxima. The threshold over the Gulf of Guinea north of the equator is also lower than in TRMM and GPCP, and approximately  $6\text{--}8 \text{ mm day}^{-1}$  lower than the threshold using the 95th percentile method (Fig. 8c). In East Africa, the model places the most intense events over the Ethiopian Highlands instead of in Kenya, southern Somalia, and Tanzania as is observed.

Because the IQR threshold is generally greater than the 95th percentile threshold in the GPCP observations, the number of extreme rainfall days is less (Fig. 9d). The exception is over Kenya, Somalia, and eastern Ethiopia where the threshold is lower and the number of days is greater. The converse is true for TRMM in general since the IQR threshold value is lower than the 95th percentile threshold value, so there is an increase in the number of extreme rainfall days (Fig. 9e). The number of extreme rainfall days in the 20C simulations (Fig. 9f) increases over the southern Sahel and equatorial Gulf of Guinea and decreases elsewhere associated with these different threshold values.

Figures 9g–i show the average rainfall intensity of extreme wet rainfall days for the observations and 20C simulations. The spatial distribution of the intensity in this method is similar to that from the 95th percentile approach, but the magnitudes differ reflecting the differences in the threshold values between the two approaches.

The comparison between the two different methods used to define extreme wet days presented above in Figs. 8 and 9 demonstrates that the methodology can affect the number and the intensity of extreme wet days calculated. Furthermore, different high-quality observations can produce significantly different results even when using the same approach. The two percentile-based approaches used here are selected because they determine the threshold value at each data point based upon the probability distribution of the individual datasets. Thus, these approaches allow for spatial comparisons because they sample the same part of the probability

distribution (Klein Tank et al. 2009). In contrast, for example, if a fixed threshold value of  $25 \text{ mm day}^{-1}$  were used, the results would not necessarily be comparable over all regions for the different datasets and model output.

Figure 10 shows the simulated differences in the number of extreme rainfall days per year for 21C–20C using the two approaches along with the percentage change. The distributions of both the differences and the percentage change fields are similar for the two different methods. The number of extreme wet days increases by  $40\%\text{--}60\%$  (4–8 days) over West Africa south of  $10^\circ\text{N}$ , by at least  $50\%$  (1–5 days) over the central and eastern Sahel, by  $50\%\text{--}90\%$  (3–7 days) over the Ethiopian Highlands, and by  $50\%\text{--}100\%$  (1–4 days) over southern Somalia, Kenya, and Tanzania. The number of extreme wet days decreases by  $30\%\text{--}60\%$  (3–6 days) over the northern Congo basin, Central African Republic, northern Cameroon, and southern Sudan. The largest differences between the two methods occurs over the northern Congo basin and southern Sudan where the negative anomalies for the IQR method (Fig. 10c) are approximately 2–3 days less than for the 95th percentile method, and along the Nigerian–Cameroon coast where the positive anomalies are 3–5 days less.

In terms of the changes in 21C extreme wet rainfall intensity (Fig. 11), the differences vary regionally and are spatially complex for both methods. The most coherent signals in both approaches include a  $30\%\text{--}70\%$  decrease in intensity over southern Niger and northeastern Mali; a  $10\%\text{--}25\%$  increase in intensity over Senegal, southern Mali, Burkina Faso, northern Nigeria, and southern Chad; and a  $25\%\text{--}75\%$  increase over the Horn of Africa.

Figure 12 shows the ensemble-mean, area-averaged number of extreme wet days per month and the ensemble member spread from the 20C and 21C simulations for the six averaging regions using the 95th percentile approach. The IQR method yields similar results (not shown). Over West Africa (Fig. 12a) the number of extreme rainfall days increases by  $10\%\text{--}30\%$  between April and October, with the largest changes in June (i.e., +0.7 day) and August (+0.45 day), which are statistically significant at the 90% and 80% intervals, respectively. The ensemble member spreads suggests that there may be an increase in the number of extreme wet days, but all six 21C ensemble members are never greater than the 20C ensemble mean for any month. The summer increase in the number of extreme wet days is consistent with Patricola and Cook (2010) who note an August–September increase in the number of late twenty-first-century extreme wet rainfall events over West Africa in their projections.

Over the Sahel (Fig. 12b) the average number of extreme wet days doubles during May. There is little change

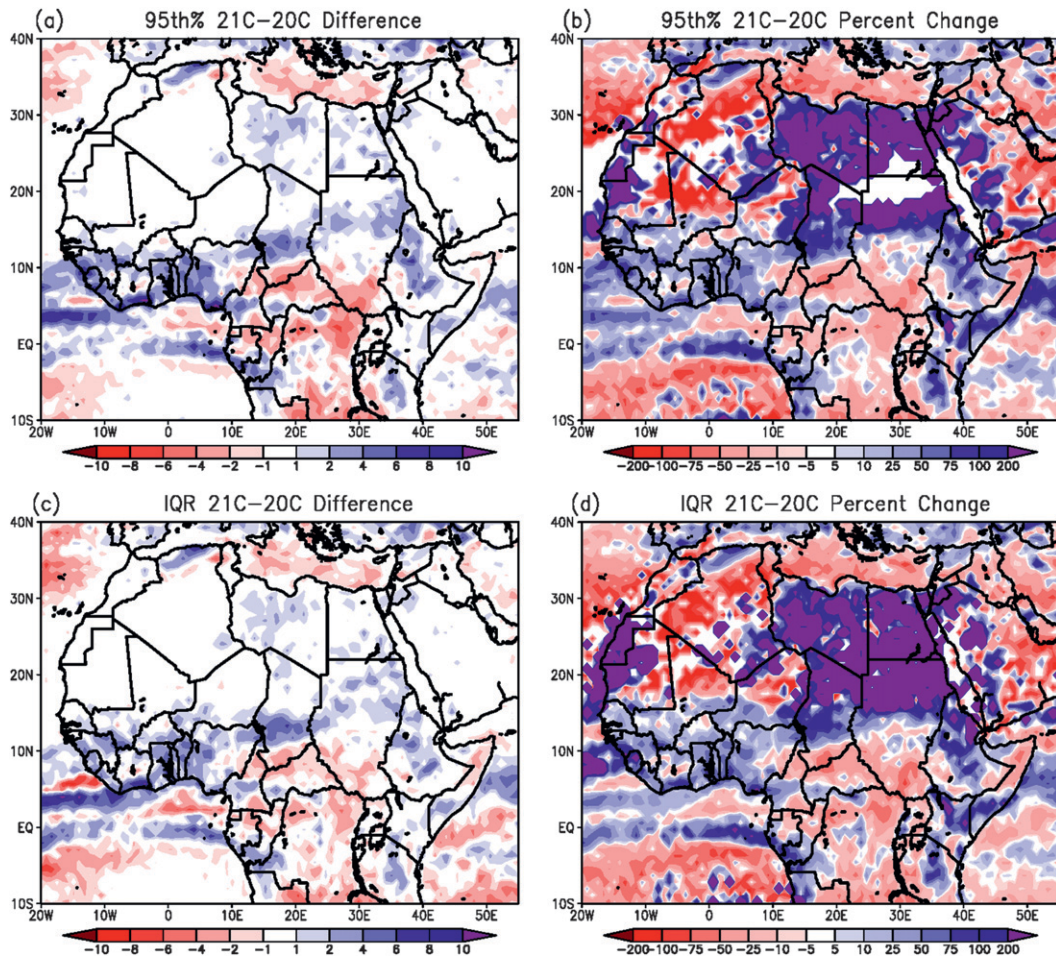


FIG. 10. Ensemble mean (a) 21C minus 20C difference and (b) 21C percentage change in the number of extreme wet rainfall days per year using 95th percentile of rainy days to identify extreme wet days. (c),(d) As in (a),(b), but they are based on using the IQR approach to identify extreme wet days.

in June, but the number of days increases by approximately 35% during July and August. Comparison of the 20C and 21C ensemble spreads indicates that not all six 21C ensemble members are greater than the 20C ensemble mean during July and August. Only July is statistically significant.

The number of extreme rainfall days decreases by 8%–28% over Central Africa (Fig. 12c) from April to September with the largest differences during April (i.e.,  $-0.35$  day) and August (i.e.,  $-0.36$  day). For this region the 21C ensemble member spread is below the 20C ensemble mean value during June and August. In April five of the six 21C ensemble members are less than the 20C ensemble mean. The changes in June, August, and October are statistically significant at the 80% confidence interval.

The response over the Sahel and Central Africa is associated with a boreal spring and late summer shift in convection farther north over the Sahel related to the

warmer climate state. Cook and Vizy (2012) show that the thermal low over the Sahara is stronger in 21C and is associated with anomalous low-level southwesterly flow that enhances moisture transport and rainfall over the central and eastern Sahel while decreasing rainfall over the Central Africa region. This change in the future rainfall pattern agrees with the mid-twenty-first-century A2 scenario projections by Vigaud et al. (2011).

There is little change in the number of extreme events during the long rains of the boreal spring over the Horn of Africa (Fig. 12d), but during the short rains of boreal fall and winter there is a 5%–30% increase. There is some separation between the 20C and 21C ensemble members in October, with almost all of the 21C ensemble members greater than the 20C ensemble mean. There is one 20C run that is three times greater than any of the other five 20C runs and this obscures the separation. The changes in April and September are statistically significant.

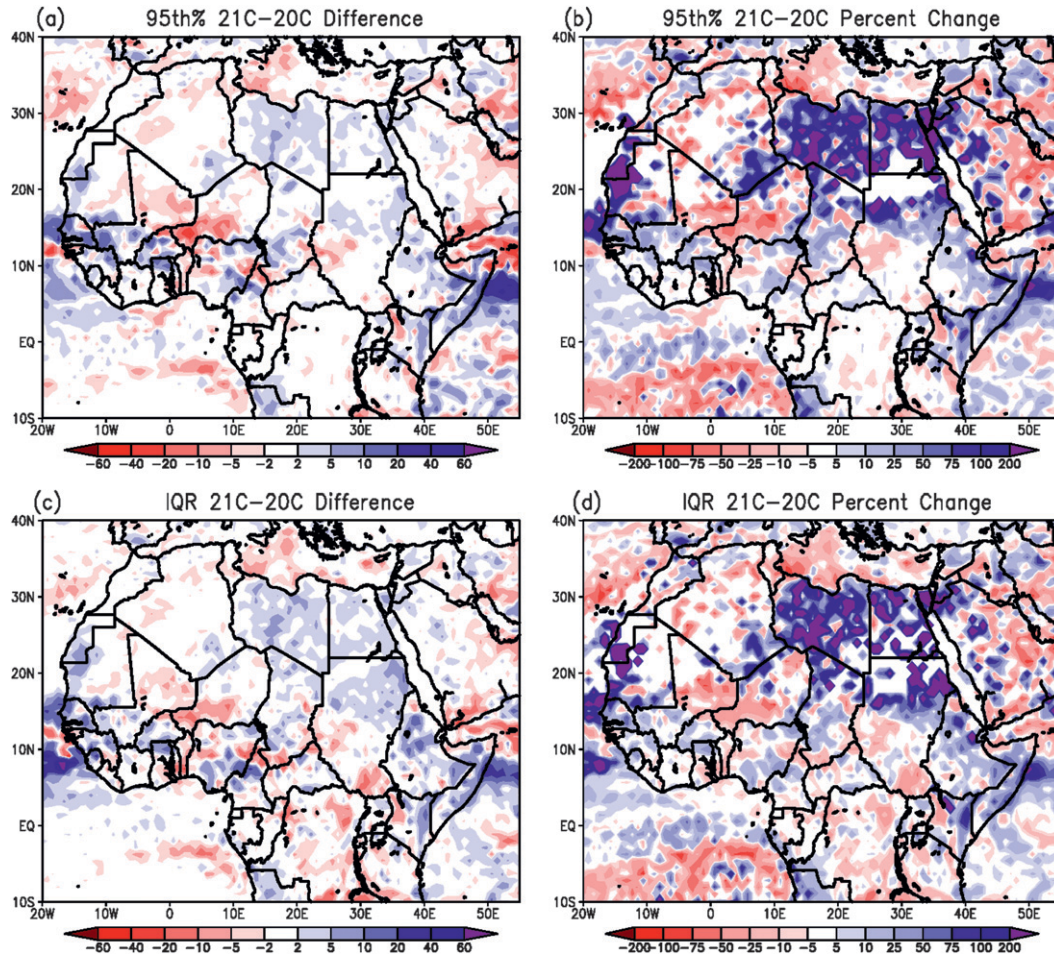


FIG. 11. Ensemble mean (a) 21C minus 20C difference ( $\text{mm day}^{-1}$ ) and (b) 21C percentage change in the extreme wet rainfall intensity per event using 95th percentile of rainy days to identify extreme wet days. (c),(d) As in (a),(b), but they are based on using the IQR approach to identify extreme wet days.

The 21C differences in the number of extreme wet days over Kenya–Tanzania (Fig. 12e) and Congo (Fig. 12f) indicate a dipole anomaly pattern. During the April and May long rains the number of extreme wet days decreases over Kenya and Tanzania by 21% ( $-0.34$  day) but increases by 30% ( $+0.78$  day) over the Congo. During the boreal fall and winter short rains this pattern reverses and the number of extreme wet days increases over Kenya and Tanzania by a factor of 4 ( $+0.62$  day) but decreases by 20% ( $-0.76$  day) over the Congo. Note that the spread between the individual ensemble members is rather large for the spring long rains over both regions with no clear separation between 20C and 21C as the changes are not highly significant. The results are more robust during fall and winter when there is separation between 20C and 21C, in particular during October over the Congo and December over Kenya and Tanzania. The September–October decrease over the Congo and the

December increase over Kenya and Tanzania are statistically significant. Cook and Vizy (2012) show that enhanced midtropospheric moisture divergence shortens the long rains season of Kenya–Tanzania, while convection farther west over the Congo basin is enhanced. This suggests that the mid-twenty-first-century long rains over Tanzania–Kenya are likely to weaken producing fewer extreme wet days, while the short rains will strengthen yielding more extreme wet days and vice versa over the Congo. This projection for the short rains agrees with the CMIP3 AOGCM predictions, which also indicate a future increase in the short rains over Kenya–Tanzania associated with changes in Indian Ocean SST gradients (Shongwe et al. 2011). Agreement is poor among the CMIP3 AOGCMs on the long rains response, however, as the AOGCMs are noted to have deficiencies in simulating precipitation during boreal spring over this region (Mutai et al. 1998; Shongwe et al. 2011).

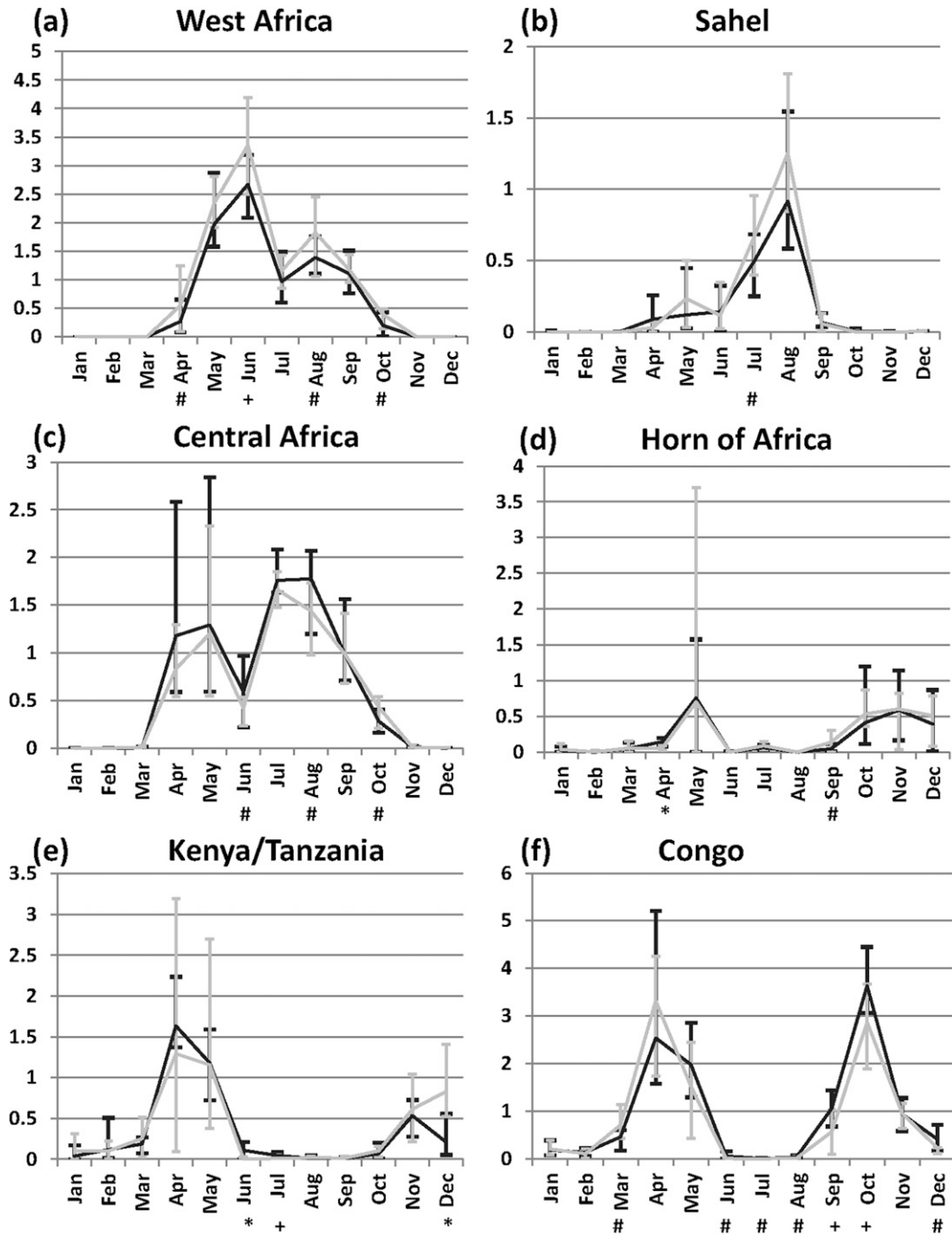


FIG. 12. 20C (black line) and 21C (gray line) ensemble mean average number of extreme heavy rainfall days per month for the (a) West Africa, (b) Sahel, (c) Central Africa, (d) Horn of Africa, (e) Kenya–Tanzania, and (f) Congo regions. Extreme heavy rainfall days are calculated using the 95th percentile of wet days to identify extreme wet days. Vertical bars denote the spread of the individual ensemble members. Monthly statistical significance is denoted by the symbols under the x axis. The #, +, and \* denote statistical significance at the 80%, 90%, and 95% confidence intervals, respectively.

To evaluate how the intensity of extreme wet rainfall days change for each region, the ensemble-mean, area-averaged total accumulated extreme wet rainfall for a given region by the ensemble mean is divided by the

area-averaged number of extreme wet days per month for the same region. Results from this calculation indicate an increase in the intensity of both the long rains (by 19% or  $7.5 \text{ mm day}^{-1}$ ) and short rains (by approximately 3%

or  $0.8 \text{ mm day}^{-1}$ ) over Kenya and Tanzania. The opposite occurs over the Congo basin with a reduction in intensity of the long rains (by 4% or  $1.14 \text{ mm day}^{-1}$ ) and short rains (by 3.9% or  $1.08 \text{ mm day}^{-1}$ ). Over West Africa the extreme wet rainfall intensity decreases by 13% ( $5.64 \text{ mm day}^{-1}$ ) in May but increases by 2%–5% from July–September. Likewise, over the Sahel the intensity is reduced by 31% ( $12.5 \text{ mm day}^{-1}$ ) in June at the beginning of the wet season but increases by 18% (7.37%) late in the wet season (September).

## 5. Summary and conclusions

A regional climate model with 90-km resolution is used to predict mid-twenty-first-century changes in climate extremes over northern and tropical Africa as the climate warms under greenhouse gas forcing. Two ensembles consisting of six members each are generated and analyzed. The first ensemble is a late-twentieth-century control that is used to assess the ability of the regional model to capture extreme weather events over Africa. The second ensemble is representative of mid-twenty-first-century (2041–60) climate under a midline emissions scenario forcing [i.e., the Special Report on Emissions Scenarios (SRES) A1B]. This target date and emissions scenario forcing are chosen to produce projections relevant for impacts analysis.

Six indicators of extreme weather are analyzed, including annual extreme temperature range, daily temperature range, the number of heat wave days, the number of dry days, the number of extreme wet days, and the extreme wet day rainfall intensity. Confidence in the projections for these measures is evaluated, based on the model's ability to simulate these extreme measures in the twentieth century and agreement among ensemble members.

Results for each extreme event indicator are summarized below.

- Annual extreme temperature range: The simulations project a widespread decrease in the annual extreme temperature range including over West Africa (0.5–1 K), the Sahel (2–3 K), and the Congo basin (up to 4 K). Both 21C maximum and minimum temperatures are projected to increase, but the magnitude of the increase is greater for the minimum temperature.
- Daily temperature range: Mid-twenty-first-century daily maximum and minimum temperatures are projected to increase in all regions analyzed, but there are regional and seasonal variations that affect the daily temperature range. The daily diurnal temperature range decreases over West Africa and Central Africa during the boreal spring and fall by 0.3–1.2 K, over the

Sahel during May–September by 0.5–1.5 K, and over the Congo basin during the boreal winter and spring by 0.5–2.0 K. Conversely, the daily diurnal temperature range increases over the Horn of Africa during the boreal winter by 0.3–1.2 K, and over Kenya–Tanzania during the boreal summer by 0.2–1.5 K associated with greater warming of the daily maximum temperature due to a decrease in atmospheric relative humidity.

- Heat wave days: A marked increase in the number of heat wave days is predicted over most of the Sahel and Saharan Africa. The number of heat wave days is projected to increase by 20–120 days over the Sahel, by 20–60 days over the Sahara west of  $15^{\circ}\text{E}$ , and by 5–40 days over the Sahara east of  $15^{\circ}\text{E}$ . There is also a projected increase in heat wave days in northernmost West Africa and central Africa averaging regions (between  $8^{\circ}$ – $11^{\circ}\text{N}$ ) primarily during boreal springtime.
- Number of dry days: The number of dry days is predicted to decrease by 15%–25% over the Congo basin and by 3%–7% over central Africa and the Sahel east of  $0^{\circ}\text{E}$  in the mid-twenty-first century. The decrease over the Congo is primarily due to a decrease in the number of dry days during the boreal winter and spring, while the reductions over Central Africa and the Sahel are associated with a decrease during the boreal spring and summer, respectively. Over East Africa, the number of dry days is projected to increase by 5%–10% and is associated with a weakening of the boreal spring long rains.
- Number of extreme wet days: The number of extreme wet days is predicted to increase over West Africa by 40%–60% (1–4 days), the southern Sahel by 50%–90% (1–4 days), and the Ethiopian Highlands by 50%–90% (2–5 days). The future increase in extreme days over the Sahel and West Africa is evenly distributed during the boreal summer months (see Figs. 12a,b). Over Somalia, the number increases by 1–4 days, but the regional model underestimates the frequency of extreme rainfall days for this region in the 20C simulation. For the Congo basin there is a 30%–60% (2–6 day) decrease in the number of extreme wet days. This decrease is associated with a reduction in extreme wet days during the short rains of the boreal fall (Fig. 12f), which is partially offset by a predicted increase in extreme wet days during the boreal spring long rains. Over Kenya and Tanzania, the projected increase in the number of extreme wet events is associated with an increase in the number of boreal fall/early winter short rain days, and is partially offset by a decrease in extreme wet days during the long rains.
- Extreme wet day rainfall intensity: The changes in extreme wet rainfall intensity are regional (Fig. 11).

The more coherent responses include a 30%–70% decrease in intensity over southern Niger and north-eastern Mali; a 10%–25% increase in intensity over Senegal, southern Mali, Burkina Faso, northern Nigeria, and southern Chad; and a 25%–75% increase over the Horn of Africa.

These results indicate a high likelihood that there will be a shift to warmer extreme temperatures by the mid-twenty-first century over sub-Saharan and tropical Africa. The severity of these changes is not uniform across the annual cycle and is regionally dependent. Heat waves, which are related to hospitalizations and death, are likely to increase not only over the Sahara and Sahel, but also to extend equatorward over tropical Africa into areas that currently do not experience such events.

Changes in extreme rainfall are regionally and seasonally dependent as well. Over West Africa both the number of dry and intense rainfall days during the boreal summer are projected to increase indicating that the summer rainfall will be delivered in fewer, but more intense events. Over the Sahel the number of extreme dry days is projected to decrease, while the number of extreme heavy rainfall days increases. Rainfall is projected to intensify over the Congo during the boreal spring and weaken in the fall and winter, with opposite results to the east over Kenya and Tanzania. These changes in extreme precipitation will have important implications for the agricultural sector as most of Africa relies on rain-fed agricultural practices. An improved understanding of how rainfall will be delivered over the annual cycle will support the development of adaptation strategies.

This study addresses issues of how to best characterize extreme rainfall in different observational and model datasets. Observational and model biases are both found to be important and can affect the uncertainty of results. Techniques used to identify extreme rainfall events based upon a dataset's own probability distribution can at least partially offset the impact of these biases and yield meaningful results, as this study demonstrates. Confidence in the results can be further strengthened by applying multiple approaches and assessing the agreement among methods.

This study is a step toward improving mid-twenty-first-century regional extreme weather projections, but there are limitations. These projections discussed above are from a single regional climate model using an ensemble approach with a limited number (6) of members. Land-use changes are not considered but could have a considerable impact over sub-Saharan Africa (e.g., Paeth and Thamm 2007). Longer integrations with more ensemble members would improve our understanding of the robustness of the predictions and their

statistical significance. Agreement with projections made by other models, both GCM and regional climate models, at comparable spatial resolutions would increase our confidence in the predictions. Another caveat is that the reanalyses and satellite-derived observations used for model validation are not in perfect agreement for the end of the twentieth century, pointing to the constant need for improved observations.

*Acknowledgments.* Discussions with our colleagues, Dr. Joshua Busby and Ms. Kaiba White, greatly improved the application and presentation of the climate model output. Support from the U. S. Army Research Laboratory Minerva Project (Contract W911NF-09-1-0077) and from the U.S. Department of Energy Office of Science (Award DE-FG02-10ER65092) is gratefully acknowledged. The Texas Advanced Computing Center (TACC) at The University of Texas at Austin provided the high-performance computing and database resources for the simulations.

#### REFERENCES

- Betts, A. K., M. Zhao, P. A. Dirmeyer, and A. C. Beljaars, 2006: Comparison of ERA40 and NCEP/DOE near-surface data sets with other ISLSCP-II data sets. *J. Geophys. Res.*, **111**, D22S04, doi:10.1029/2006JD007174.
- Chen, F., and J. Dudhia, 2001: Coupling an advanced land-surface/hydrology model with the Penn State/NCAR MM5 modeling system. Part I: Model description and implementation. *Mon. Wea. Rev.*, **129**, 569–585.
- Chen, S.-H., and W.-Y. Sun, 2002: A one-dimensional time dependent cloud model. *J. Meteor. Soc. Japan*, **80**, 99–118.
- Cook, K. H., and E. K. Vizy, 2012: Impact of climate change on mid-twenty-first century growing seasons in Africa. *Climate Dyn.*, doi:10.1007/s00382-012-1324-1, in press.
- Dudhia, J., 1989: Numerical study of convection observed during the winter monsoon experiment using a mesoscale two-dimensional model. *J. Atmos. Sci.*, **46**, 3077–3107.
- Frich, P., L. V. Alexander, P. Della-Marta, B. Gleason, M. Haylock, A. M. G. Klien Tank, and T. Peterson, 2002: Observed coherent changes in climatic extremes during the second half of the twentieth century. *Climate Res.*, **19**, 193–212.
- Hagos, S. M., and K. H. Cook, 2007: Dynamics of the West African monsoon jump. *J. Climate*, **20**, 5264–5284.
- Hong, S.-Y., Y. Noh, and J. Dudhia, 2006: A new vertical diffusion package with an explicit treatment of entrainment processes. *Mon. Wea. Rev.*, **134**, 2318–2341.
- Kain, J. S., 2004: The Kain-Fritsch convective parameterization: An update. *J. Appl. Meteor.*, **43**, 170–181.
- Kalkstein, L. S., and K. E. Smoyer, 1993: The impact of climate change on human health: Some international implications. *Experimentia*, **49**, 44–64.
- Kanamitsu, M., W. Ebisuzaki, J. Woollen, S. K. Yang, J. J. Hnilo, M. Fiorino, and G. L. Potter, 2002: NCEP-DOE AMIP-II Reanalysis (R2). *Bull. Amer. Meteor. Soc.*, **83**, 1631–1643.
- Kharin, V. V., F. W. Zwiers, X. Zhang, and G. C. Hegerl, 2007: Changes in temperature and precipitation extremes in the

- IPCC ensemble of global model simulations. *J. Climate*, **20**, 1419–1444.
- Klein Tank, A. M. G., F. W. Zwiers, and X. Zhang, 2009: Climate data and monitoring. WCDMP-72, WMO-TD 1500, 56 pp.
- Meehl, G. A., and Coauthors, 2007: Global climate projections. *Climate Change 2007: The Physical Science Basis*, S. Solomon et al., Eds., Cambridge University Press, 747–845.
- Mlawer, E. J., S. J. Taubman, P. D. Brown, M. J. Iacono, and S. A. Clough, 1997: Radiative transfer for inhomogeneous atmosphere: RRTM, a validated correlated-k model for the longwave. *J. Geophys. Res.*, **102** (D14), 16 663–16 682.
- Moore, D. S., and G. P. McCabe, 1993: *Introduction to the Practice of Statistics*. W. H. Freeman and Company, 854 pp.
- Mutai, C. C., M. N. Ward, and A. W. Colman, 1998: Toward the prediction of the East African short rains passed on sea surface temperature and atmosphere coupling. *Int. J. Climatol.*, **18**, 975–997.
- Paeth, H., and H.-P. Thamm, 2007: Regional modeling of future African climate north of 15°S including greenhouse warming and land degradation. *Climatic Change*, **83**, 401–427.
- , K. Born, R. Girmes, R. Podzun, and D. Jacob, 2009: Regional climate change in tropical and northern Africa due to greenhouse forcing and land use changes. *J. Climate*, **22**, 114–132.
- , and Coauthors, 2011: Progress in regional downscaling of West African precipitation. *Atmos. Sci. Lett.*, **12**, 75–82.
- Patricola, C. M., and K. H. Cook, 2007: Dynamics of the West African monsoon under mid-Holocene precessional forcing: Regional climate model simulations. *J. Climate*, **20**, 694–716.
- , and —, 2010: Northern African climate at the end of the twenty-first century: An integrated application of regional and global climate models. *Climate Dyn.*, **35**, 193–212.
- , and —, 2011: Sub-Saharan Northern African climate at the end of the twenty-first century: Forcing factors and climate change processes. *Climate Dyn.*, **37**, 1165–1188.
- Robinson, P. J., 2001: On the definition of a heat wave. *J. Appl. Meteor.*, **40**, 762–775.
- Shongwe, M. E., G. Jan Van Oldenborgh, and B. Van Den Hurk, 2011: Projected changes in mean and extreme precipitation in Africa under global warming. Part II: East Africa. *J. Climate*, **24**, 3718–3733.
- Skamarock, W. C., J. B. Klemp, J. Dudhia, D. O. Gill, D. M. Barker, W. Wang, and J. G. Powers, 2005: A description of the advanced research WRF version 2. NCAR/TN-408+STR, 88 pp. [Available from NCAR Information Services, P.O. Box 3000, Boulder, CO 80307.]
- Steadman, R. G., 1979: The assessment of sultriness. Part I: A temperature humidity index based on human physiology and clothing science. *J. Appl. Meteor.*, **18**, 861–873.
- , 1984: A universal scale of apparent temperature. *J. Climate Appl. Meteor.*, **23**, 1674–1687.
- Sylla, M. B., A. T. Gaye, G. S. Jenkins, J. S. Pal, and F. Giorgi, 2010: Consistency of projected drought over the Sahel with changes in monsoon circulation and extremes in a regional climate model projections. *J. Geophys. Res.*, **115**, D16108, doi:10.1029/2009JD012983.
- Tebaldi, C., K. Hayhoe, J. M. Arblaster, and G. A. Meehl, 2006: Going to the extremes: An intercomparison of model-simulated historical and future changes in extreme events. *Climatic Change*, **79**, 185–211.
- Vigaud, N., P. Roucou, B. Fontaine, S. Sijikumar, and S. Tyteca, 2011: WRF/ARPEGE-CLIMAT simulated climate trends over West Africa. *Climate Dyn.*, **36**, 925–944.
- Vizy, E. K., and K. H. Cook, 2002: Development and application of a mesoscale climate model for the tropics: Influence of sea surface temperature anomalies on the West African monsoon. *J. Geophys. Res.*, **107**, 4023, doi:10.1029/2001JD000686.
- , and —, 2003: Connections between the summer East African and Indian rainfall regimes. *J. Geophys. Res.*, **108**, 4510, doi:10.1029/2003JD003452.
- Vose, R. S., D. R. Easterling, and B. Gleason, 2005: Maximum and minimum temperature trends for the globe: An update through 2004. *Geophys. Res. Lett.*, **32**, L23822, doi:10.1029/2005GL024379.
- Zhang, X., and F. Yang, 2004: RCLIMDEX (1.0) user manual. Climate Research Branch, Environment Canada, 23 pp. [Available online at <http://precis.metoffice.com/Tutorials/RCLIMDEXUserManual.doc>.]